Sulfidation of major rock types of the oceanic lithosphere; An experimental study at 250 °C and 400 bars

Catharina Los [a,*], Wolfgang Bach [a,b]

[a] Geosciences Department, University of Bremen, Klagenfurter Str. 2, 28359 Bremen, Germany
[b] MARUM, Center for Marine and Environmental Sciences, Leobener Str., 28359 Bremen, Germany

ARTICLE INFO

ABSTRACT

Circulation of hydrothermal fluids within the oceanic crust is a major factor in mass and heat transfer between hydrosphere and lithosphere. Many occurrences of massive sulfide have been reported along the mid-ocean ridges, showing effective mass transfer of sulfur and metals in these systems. Besides precipitation of sulfide at the seafloor, replacive sulfide formation in the sub-seafloor has been documented. However, different lithologies are expected to have different affinities to sulfidization. To investigate the role of rock composition on sulfidization efficiency, we have conducted batch experiments at 250 °C and 400 bars that placed an H_2S-rich hydrothermal fluid into contact with four different rock types: dunite (olivine separates), troctolite, basalt, and serpentinite. These rocks were exposed to fluids containing 20 mmol/kg total dissolved sulfide for durations between 1 and 10 weeks. *In situ* fluid sampling allowed us to determine the evolution of the concentrations of ionic solutes and dissolved gases. Solid products were analyzed after termination of the experiments, using XRD, SEM, TG and VSM. Geochemical modeling was employed to compare observed reaction with equilibrium thermodynamic predictions.

Sulfide (in the form of euhedral pyrite crystals) could be observed only in the basalt experiment. In all other runs, prevailing H_2S-activities were too low for sulfide formation despite high total sulfide concentrations. Instead, the troctolite and peridotite experiments showed serpentinization of olivine and magnetite formation. Plagioclase in troctolite experienced desilicification, resulting in andradite formation. The stability field of sulfide in the H_2-H_2S activity plane is diminished due to the prevalence of andradite in hydrothermally reacted troctolite and sulfidization in the troctolite experiment was hence inhibited. The serpentinite experiment showed very little reaction and no sulfide formation. Our results show that olivine-rich seafloor lithologies are not very prone to sulfidation; basaltic crust appears to have a larger potential to form sulfide deposits. In some experiments, pyrrhotite did not form although H_2-H_2S activities plot in the pyrrhotite stability field of the Fe-O-S phase diagram. We suggest that the higher oxidation state in basalt allows for the precipitation of pyrite, which is not stable under the more reducing conditions prevailing where water interacts with olivine-rich lithologies.

1. Introduction

Hydrothermal fluid circulation within the oceanic lithosphere plays a large role in mass and heat transfer on Earth. Rock alteration can occur through exposure to magmatic fluids and percolating seawater close to spreading ridges, by infiltration of seawater in (deep) fractures or by the development of core complexes (e.g., Melchert et al., 2008; Petersen et al., 2009; Smith et al., 2008). The reactive fluid leaches out fluid mobile elements, which are re-deposited upon cooling and oxidation when the fluid ascends to the ocean floor (Seewald and Seyfried, 1990). Local enrichments of heavy metals such as Fe, Cu, Zn and Ni are often captured within sulfide minerals. Sulfide formation therefore depends on sulfur activity in the fluid, fluid pathways and the vicinity to a hydrothermal vent system. Although many sulfide-bearing root zones are discovered, not all rock types have the same potential to form massive sulfide deposits.

Sulfide is present in minor amounts in most lithologies exposed at the seafloor, displaying its stability in the oceanic lithosphere. In basalts or gabbros sulfides often have a magmatic origin (Czamanske and Moore, 1977; Peach et al., 1990), which is visible in sulfur isotopes. Altered rocks show more mixed signatures (e.g., Alt and Shanks, 2011; Delacour et al., 2008a; Peters et al., 2010), implying a seawater source for additional S or leaching of primary sulfides from the system through hydrothermal processes. One sulfur enrichment process leading to hydrothermal sulfide formation is thermochemical sulfate reduction above 250 °C, which has been suggested to be driven by protons released from Mg-metasomatism (Shanks II et al., 1981). At lower

* Corresponding author.
  E-mail address: karinlos91@gmail.com (C. Los).

temperatures abiotic sulfate reduction is kinetically sluggish and seawater sulfate reduction is catalyzed microbially (Alt et al., 2013; Alt and Shanks III, 1998; Delacour et al., 2008a; Schwarzenbach et al., 2012). Deeper sections of the lithosphere consist of ultramafic rock types such as plagioclase-bearing troctolites, as seen in IODP hole 1309D, where not many sulfides are reported (Alt et al., 2007; Delacour et al., 2008b; Früh-Green et al., 1996). Instead, metals are commonly stored in spinels or as oxides. Hydrothermal circulation can destabilize these minerals and dissolve them, increasing metal content in the fluid. One example of hydrothermal alteration is the hydration of peridotite, manifested as serpentinization (Seyfried Jr. and Dibble Jr., 1980; Godard et al., 2013; Klein et al., 2015; and others). During this process, magnetite forms and high amounts of H_2 are produced, causing de-sulfidation of the ultramafic rock (Frost, 1985; Klein and Bach, 2009). The resulting release of H_2S and subsequent transport may result in the precipitation of sulfide phases close to the seafloor (Alt and Shanks III, 2003; Bach et al., 2004; Delacour et al., 2008b). At this shallow level close to discharge, especially sharp changes in pH, temperature and oxidation state destabilize metal complexes formed with Cl^- or HS^- (Seward et al., 2014) resulting in sulfide precipitation. Sulfides can also form replacively, postdating other alteration events and overprinting preexisting alteration textures (Marques et al., 2006, 2007).

In the case of replacement of the host rock by sulfides, an ore body with a high metal concentration can form. Such sulfide deposits have been discovered along many plate boundaries in all exposed lithologies of the oceanic lithosphere. Especially freshly formed basalt is well known to host large amounts of pyrite, a relatively oxidized sulfide phase that is found here surrounded by zones of silicification, chloritization and sericitization (upflow zone of TAG, Humphris et al., 1995). This pyrite is often enriched in trace elements through zone refining processes (Hannington et al., 1998). At depth, pyrite fragments are cemented either by anhydrite (shallow) or quartz (deeper sections). In the upflow zone, sulfidation can actually replace wall rock or create sulfide-bearing veins, observed both in drill cores (Bach et al., 2004; Hannington et al., 1998) and ophiolite sections (Adamides, 2010; Zierenberg et al., 1988).

Several experimental studies have looked into seawater-rock interaction and replacive sulfide formation. Bischoff and Dickson (1975) showed that at 200 °C, seawater-basalt interaction decreased fluid pH because Mg-metasomatism released H^+ from the rock. Simultaneous Mg-Ca exchange resulted in precipitation of sulfate as anhydrite (Mottl and Holland, 1978). Mottl et al. (1979) found anhydrite and additional pyrite or pyrrhotite at 300 °C and 400 °C; these sulfide phases were also observed in experimental runs where no sulfate was added in solution. The authors linked sulfate reduction to ferrous iron oxidation. Shanks II et al. (1981) tested this iron oxidation with fayalite-seawater experiments at 250 °C and 350 °C and different water-to-rock (w/r) ratios. They found that at low w/r ratios (<50), pyrrhotite and magnetite formed while at higher ratios, more oxidizing conditions prevailed and pyrite, hematite and anhydrite were present. These examples show that sulfur plays a large role in alteration of the oceanic crust and that more study on sulfidation is needed.

This communication looks at the potential of different lithologies to form sulfide minerals upon interaction with sulfide-bearing solutions, focusing on sulfidation in the subsurface close to discharge. We conducted experiments that placed basalt, troctolite, serpentinite and pure olivine (to resemble peridotite protolith) in contact with an H_2S-rich solution representing a black smoker vent fluid with a low HS^-- metal complexing ability. Our experiments used the same fluid with 20 mmol/kg H_2S for all rock types in order to distinguish the rock potential, with different w/r ratios. In natural systems, the w/r ratio rarely exceeds 10 except right next to a discharge area with high upflow rates. However, as a high w/r ratio oxidizes the system and the used fluid adds large quantities of sulfur, it represents the most favorable conditions to form pyrite that we could test. Although natural systems are subjected to temperatures between 250 and 400 °C, we used a reaction temperature of 250 °C, which ensured a pressure tight experimental setup. Both the solid reaction products and the composition of the reaction fluids (including dissolved gases) were analyzed in order to determine the rock potential; this was then compared to modeled thermodynamic mineral stability.

2. Methods

2.1. Experimental setup

In order to simulate water-rock reactions under hydrothermal conditions close to discharge, a powdered (75–150 μm fraction) rock sample and N_2-purged de-oxygenized milliQ-water were weighed in a flexible gold cell (volume of roughly 100 mL). NaOH was added to acquire a fluid pH of 9–9.5 at 250 °C where the H_2S-fraction of total sulfur $\sum S$ is modeled to be highest (1%). This was done to reduce metal solubility by HS^- complexing, also kept to a minimum by low salinity (no addition of NaCl). Na_2S-flakes were added to this fluid and the cell was closed immediately after with a titanium ring attached to a pressure vessel. A tube connected to a valve at the top of the autoclave allowed us to sample the fluid during the reaction. The flexible gold cell was flushed with nitrogen and the headspace of the valve was emptied using this pressure. The autoclave was filled with water and closed tightly. This water was pressurized with air and the whole setup was placed within a heater. Two thermocouples (at top and bottom of the pressure vessel) monitored temperature in the reaction cell, which was set to 250 °C. During heating, the pressure increased by expansion of the fluid within the pressure vessel; we decompressed when it exceeded 420 bars. When 250 °C was reached, the system stabilized and pressure was kept constant around 400 bars for 1–10 weeks depending on the H_2 produced by the ongoing reaction. At 400 bar and 250 °C, H_2 solubility in mildly salty solutions is very high (Sleep et al., 2004) and all H_2 produced is dissolved in the fluid (H_2,aq). Activities of H_2 and H_2S were calculated from measured concentrations of H_2 and $\sum S$, assuming unity activity coefficients. Because the aim of this study was to form sulfide minerals, the reaction was stopped when conditions moved outside the pyrite or pyrrhotite stability field. For the experimental setup, see Fig. 1 from Shibuya et al. (2013).

2.2. Different experiments

Five experiments were run, listed below with starting pH at 25 °C:

The very first basalt experiment was shut down after one day due to pressure loss. Basalt: 5.205 g rock, 74.968 mL fluid, 223 mg Na_2S, fluid pH of 9.5, ran for 63 days;

Troctolite: 4.486 g rock, 72.385 mL fluid, 198 mg Na_2S, fluid pH 11.0, ran for 49 days;

Olivine: 0.898 g rock, 74.606 mL fluid, 192 mg Na_2S, fluid pH 11.5, ran for 9 days;

Serpentinite: 0.788 g rock, 73.462 g mL fluid, 181 mg Na_2S, fluid pH 10.5, ran for 11 days. The run was stopped when H_2(aq) moved deep into the pyrrhotite field. After termination of each experiment, solids were removed and centrifuged in milliQ-water to remove reaction fluid and salt build-up, and then dried under vacuum.

2.3. Analyses

Fluid samples were taken by carefully opening the pressure valve. After removal of the headspace of the valve (1.5 mL) an airtight syringe was used to capture 1 mL of fluid. Dissolved gases in the basalt experiment were measured using a 7820A Agilent Gas-Chromatograph (GC) equipped with a thermal conductivity detector (TCD) for H_2, led through a Molsieve 60/80 column with N_2 as carrier gas. Measured standards contained 1.031 vol% H_2, 1.031 vol% CO, 1.012 vol% CO_2 and 0.996
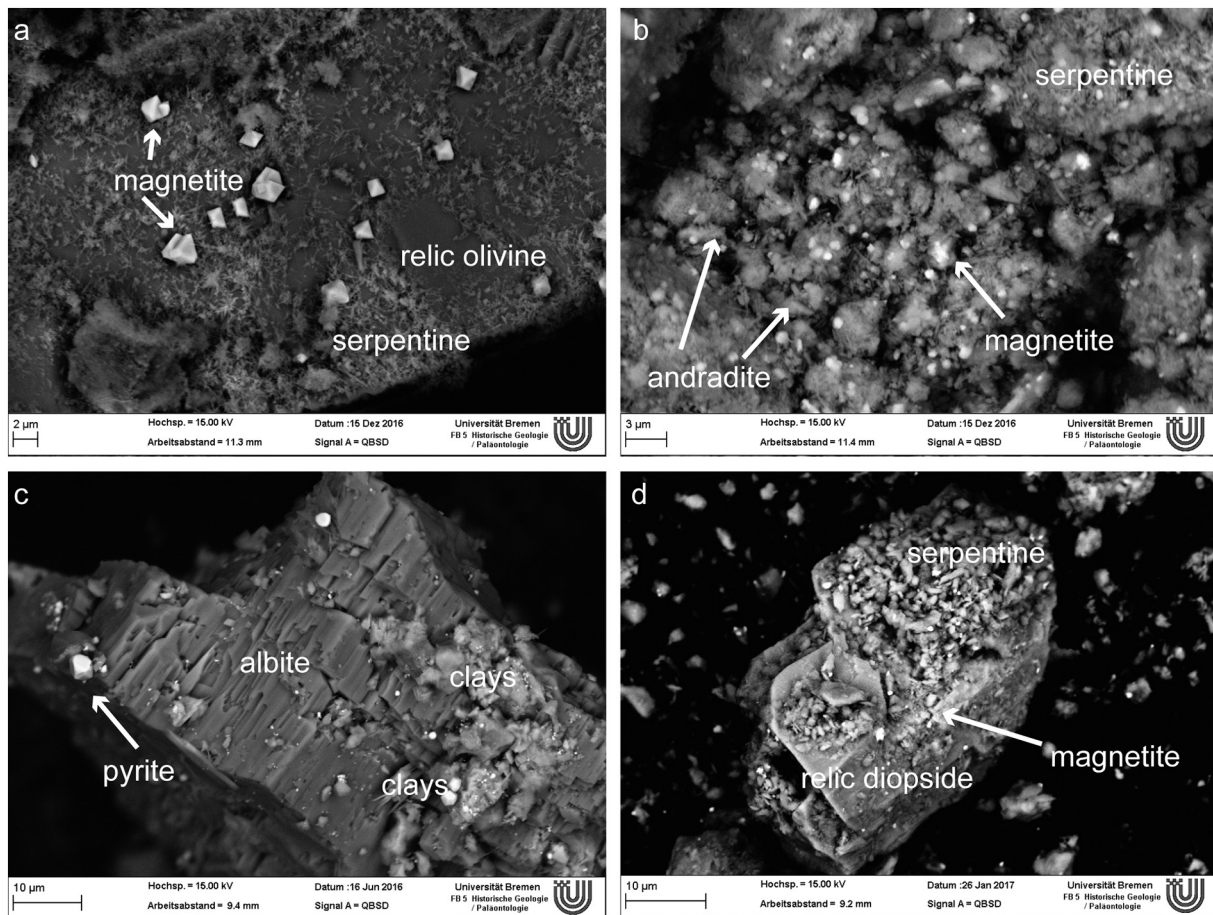
Fig. 1. SEM images of reaction products of olivine (a), troctolite (b), basalt (c) and serpentinite (d) experiment. All samples show only superficial alteration; cuts through the grains only show primary minerals.

vol% CH_4. For the other experiments, a Peak Performer 1 was used and a standard with 10 ppm H_2 and CO; the taken samples were diluted to fall within the range calibrated by the standard. Major element chemistry was measured on fluid samples diluted with 1% HNO_3 using Inductively Coupled Plasma – Optical Emission Spectroscopy (ICP-OES) of the type Varian Vista using 3 standards to calibrate (Konz, VF2, VF10). These measurements were performed on the degassed samples after GC-measurement in order to maximize the use of fluid samples, since every sample decreased the water-to-rock ratio within the gold cell. For dissolved H_2S an additional sample was taken where all sulfur was fixated directly with zinc-acetate; this sample was measured using a Dr5000 Photometer.

Solids were analyzed using a Supra 40 Scanning Electron Microscope (SEM) with an XFlash 6/30 Energy Dispersive X-ray (EDX)-detector (15 kV) or with electron microprobe analysis (EMPA) using a Cameca SX100 (20 kV, 1 μm beam size) on the starting material. Thermogravimetry was done using a Netzsch DTA-TG machine using a heating rate of 10 K/min. X-ray powder diffraction (XRD) analysis was performed on bulk starting and product materials using a Philips X'Pert Pro multipurpose diffractometer equipped with a Cu-tube ($k_α$ 1.541, 45 kV, 40 mA), a fixed divergence slit of ¼°, a 16 samples changer, a secondary Ni-Filter and the X'Celerator detector system. An Axios Plus of Panalytical was used for X-ray Fluorescence bulk rock data, at ICBM in Oldenburg, Germany (see Table 1 for bulk and mineral compositions) just on starting material. This technique was performed on glass pellets and data quality was checked using a PS-S black shale standard; detection limits were never higher than 0.03 wt%; the average error was 0.1 wt%.

Magnetic properties were measured at the Norwegian University of Science and Technology (NTNU). High and low temperature magnetic susceptibility was measured using an Agio MFK1-A Kappabridge with CS4 and CS-L units, respectively, analyzing the type of magnetic mineral looking for the Curie temperature (high temperature) and possible Verwey transition (low temperature) if the mineral was magnetite. To quantify this magnetic phase, saturation magnetization (which increases linearly with the amount of magnetic mineral) was determined using hysteresis loops and high temperature magnetic measurements performed with a Princeton Measurements Corporation MicroMag 3900 Vibrating Sample Magnetometer (VSM). This value was corrected for linear paramagnetic slope and the curves were further analyzed using the Igor software package.

2.4. Modeling

To predict geochemical behavior and mineralogical changes, the EQ3/6 work package (Wolery and Jarek, 2003) was used. A database for 500 bars was constructed; equilibrium constants were determined using SUPCRT92 (Johnson et al., 1992) while activity coefficients were calculated using the Debye-Hückel equation. In these models, the starting material was entered as a special reactant whose composition was derived from XRF-data on the materials used. Ferrous iron components were taken to be 0.8–0.9 for the mafic rock types and 0.33 for the serpentinite (as in the mineral magnetite, or whole rock data by Paulick et al., 2006). Different w/r ratios were modeled (10, 20, 50, 100) in order to find the best conditions for sulfide formation. This outcome was used to calculate the amount of sample that should be added to the fluid.

Table 1
Bulk rock and average mineral compositions.

Sample	San Carlos olivine	1309D Troctolite			Basalt				Serpentinite
Data type	Bulk rock	Bulk rock	Mineral	Mineral	Bulk rock	Mineral	Mineral	Mineral	Bulk rock
			Olivine	Plagioclase		Feldspar	Clinopyroxene	Chlorite	
SiO$_2$	40.81	41.06	39.55	47.79	49.03	57.86	50.55	30.84	37.21
Al$_2$O$_3$		5.39	0.04	30.7	15.39	27.08	1.6	17.37	4.97
FeO, total	9.55	12.21	13.79	0.92	9.17	0.99	14.59	38.42	14.48
MgO	49.42	34.18	46.24	0.95	7.94	0.27	12.67	12.54	26.44
CaO	<0.05	3.52	0.08	16.84	10.91	4.6	19.28	0.27	2.45
Na$_2$O		0.57	0.02	2.68	2.86	5.35	0.31	0.16	0.04
K$_2$O		0	0.01	0.02	0.23	3.76		0.02	0.07
TiO$_2$		0.072	0.01	0.04	1	0.06	0.62	0.05	0.51
P$_2$O$_5$	0	0.009			0.14				0.07
MnO	0.14	0.19	0.25	0.05	0.17	0.03	0.36	0.31	0.2
Cr$_2$O$_3$			0.01	0.01			0.03	0.01	
Total	100.29	97.20	97.95	97.36	97.31	100.2	100.48	88.91	86.44
Source	Jarosewich et al. 1980	XRF	EMPA	EMPA	XRF	EMPA	EMPA	EMPA	XRF

The predicted mineral stability in the Fe-O-S system at 250 °C and 400 bars was plotted in an activity-activity diagram, using Log a H$_2$S vs. Log a H$_2$ as axis variables. The changing w/r ratio during the experiment was not taken into account because reaction time could not be accurately estimated due to unknown kinetic variables. Instead, modeled reactions were allowed to run to the end, and at several w/r ratios because this ratio changed during the run. The changing ratio limited the number of possible samples; subtracting too much fluid would move the system out of the preferred stability field.

Speciation of measured total sulfur in the fluid samples was predicted using the EQ3/6 software to calculate H$_2$S-activity, assuming an activity coefficient of 1 since these species have neutral charge. The computed H$_2$S activities are highly sensitive to pH in our experiments because the in situ pH values are similar to – or slightly greater than – the pK$_s$ of H$_2$S, and hence HS$^-$ is commonly the dominant sulfide species. To illustrate the resulting mineral stability fields in an activity-activity plot, Geochemists Work Bench (Wolery and Jarek, 2003) was used.

3. Results

We have executed 4 successful runs with duration of 1–10 weeks each. The reacted material has been imaged using SEM (Fig. 1a–d) and major fluid chemistry is given in Fig. 2a–e and Table 2. H$_2$ and H$_2$S fugacity during reaction progress are also shown in Table 2 and in Fig. 3 along with the modeled stable mineral phase in the Fe-O-S system.

3.1. Olivine

San Carlos olivine (Fo$_{90}$; for composition, see Table 1) was allowed to react with fluid at a w/r ratio of 83, leading to serpentinization with the formation of serpentine, brucite and magnetite (Fig. 1a).

Olivine dissolution is visible from increasing dissolved Si shortly after the reaction started, and its slight decrease after 1 day coincides with serpentine formation. Mg, Ca, Fe and Al also decrease slightly during the reaction while Si and K remain roughly constant in the output fluid (Fig. 2a); Ca and K are likely introduced to the system as trace amounts in the Na$_2$S-flakes. Fe is partially taken up in serpentine and in magnetite but some remains in the fluid; the presence of only 0.1 wt% magnetite detected with the VSM coincides with roughly 5% serpentinization, consistent with the small amount of weight loss at the 600 °C serpentine dehydration point in thermogravimetry.

During the run, an increasing amount of H$_2$ was released as olivine serpentinization proceeded through the oxidation of ferrous iron (Klein et al., 2009). Measured H$_2$ and inferred H$_2$S concentrations in the output fluid show that the system plots within the pyrrhotite field (Fig. 3). However, only upon cooling at the end of the experiment,

a 6 mmol/kg decrease in $\sum$ S content is seen in the output fluid (Fig. 2e), suggesting the possible formation of pyrrhotite. This drop in dissolved sulfur would coincide with 0.50 mmol S or 42.4 mg pyrrhotite; this is 0.5% of the sample weight, explaining its invisibility.

3.2. Troctolite

Troctolite from IODP Hole 1309D (core 248R-2 15-17 cm, retrieved at 1193.6 mbsf) consisted of 25% anorthite-rich plagioclase and 75% olivine (Table 1); the main reaction products detected using XRD are lizardite (70%), andradite (10%), saponite (10%) and magnetite (5%) as also seen in the SEM image (Fig. 1b); no relic olivine or plagioclase was observed. The experiment started with a w/r ratio of 16.5.

An initial peak in the release of Al, Fe, Mg, Ca, K and Si showed simultaneous dissolution of olivine and plagioclase (Fig. 2b), but their fluid concentrations decreased again upon incorporation in the main secondary minerals, Mg disappearing completely from the output fluid. Na is not taken up in any phase (Fig. 2e). The detection of minor anatase (TiO$_2$) and cristobalite (SiO$_2$) in XRD shows supersaturation and precipitation of these phases.

This experiment shows olivine hydration and thus releases large amounts of H$_2$ during the run. Consequently, the fluid compositions plot within the pyrrhotite and later the magnetite field (Fig. 3, blue stars), but again pyrrhotite is not observed with any of the used techniques.

Dissolved sulfide first increased to 28 mmol/kg and decreased during the run to 24 mmol/kg after 20 days (Fig. 2e). After that, sulfur content in the fluid was seen to increase slightly again. This changing S-content during reaction could be interpreted as redissolution of pyrrhotite, releasing S and Fe to the solution. A simultaneous Fe peak suggests this as well but a later decrease after 30 days shows that Fe might be captured in magnetite and hydrogarnet (andradite).

3.3. Basalt

Optical microscopy and XRD on the basaltic starting material were used to estimate the proportions of the major phases including plagioclase (58%), clinopyroxene (20%) and chlorite (15%) and minor phases such as apatite and spinel. The starting w/r ratio was 14.

Fluid data show the rapid increased Si and Al at early stages of reaction, with some K and Ca (Fig. 2c). This accounted for the dissolution of plagioclase. Aluminum contents in the fluid quickly decreased while Si remained elevated. One possible sink of Al may be the observed analcime (NaAlSi$_2$O$_6$·H$_2$O), as Na also decreased very quickly in the fluid (Fig. 2e). A simultaneous drop in dissolved S and Fe recorded the formation of pyrite (see Fig. 1c). Later decreasing Mg and Ca after 28 days (w/r ratio of 13 at that point due to fluid extraction by sampling) could be
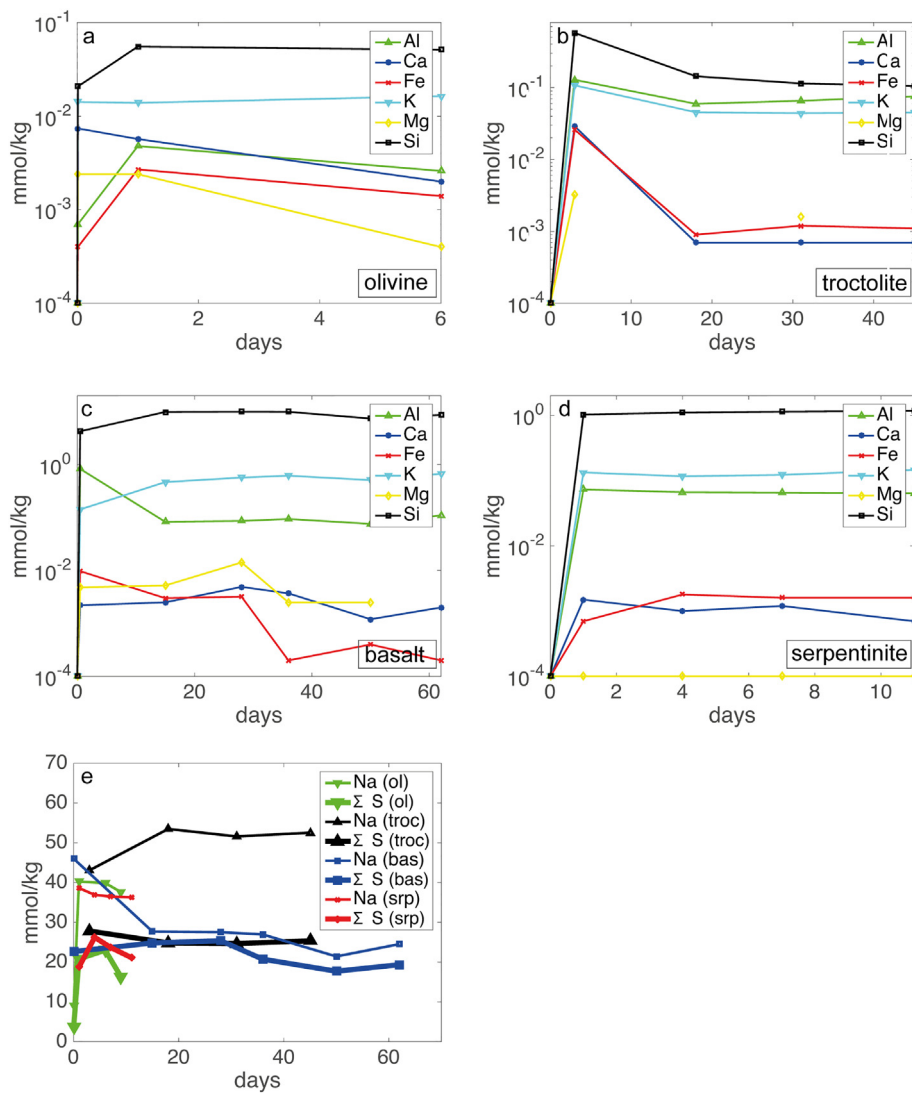
Fig. 2. Major element concentrations in fluids from olivine (a), troctolite (b), basalt (c) and serpentinite (d) experiment; (e) shows the different $\sum S$ (solid line) and Na (dotted line) changes in all experiments, where olivine is represented by downward triangles, troctolite by upward triangles, basalt by squares and serpentinite by crosses. Note the similar trend for olivine and serpentinite.

captured in tremolite or epidote, but due to the small amounts of Ca released (total of 5 μmol in solution) this would not result in detectable amounts. Minerals found in the reacted specimen using XRD and electron microscopy include clinopyroxene (27%), plagioclase (55%), chlorite (9%), clays (8%), analcime and pyrite (both below detection limit in XRD). This shows that the reaction did not go to completion as relic pyroxene and feldspar phases make up more than half of the sample volume.

Measured gas concentrations are consistent with the formation of pyrite (black circles in Fig. 3). During reaction, an increasing amount of H_2 was produced, slowly shifting the reaction into the pyrrhotite field. However, the last measurement point is again situated within the pyrite field and no evidence for the presence of pyrrhotite is found, either with SEM, VSM or XRD. Low temperature alteration phases like clays can be due to cooling artifacts before opening of the reaction cell.

3.4. Serpentinite

The reaction of serpentinite rock (roughly 80% serpentine minerals and minor magnetite, Ni-Co-sulfides and pyroxene and some olivine relics, based on optical and electron microscopy) with H_2S-rich fluid

was expected to be relatively close to equilibrium, since the reaction of olivine with the same fluid resulted in serpentinite. The starting w/r ratio was 93, as to have very oxidizing conditions and a large amount of sulfur added to the system.

The resulting serpentine and magnetite product minerals (Fig. 1d) seen in the SEM still closely resemble the starting material. Unlike in all other experiments, released major element ions in the fluid samples did not decrease with reaction progress. Instead, they remained constant or even increased slightly (see Si in Fig. 2d). This is consistent with the idea that this reaction is already close to equilibrium from the start. The only ions to decrease during the reaction are the ones added to the system, Na and S (decrease of 3 mmol/kg, corresponding to 0.225 mmol in the present 75 mL in the gold cell), and they are close to the amounts for the olivine experiment (Fig. 2e). It is most likely that these elements are incorporated into clay minerals and a sulfide phase, respectively, when relic olivine and pyroxene are serpentinized (Fig. 2d). However, once again no pyrrhotite is observed despite the dissolved gas concentrations showing favorable conditions for its formation (red squares in Fig. 3). Instead, minor amounts of newly grown magnetite are present, along with Ni- and Co-bearing sulfide minerals. These minerals were not taken into consideration for the reaction path model due to their small quantities, but they might play a role in

Table 2
Measured fluid chemistry for all samples, including dissolved gas content, given in mmol/kg. N.d is not detected.

Experiment	Olivine			Troctolite					Basalt						Serpentinite			
Time (days)	0	1	6	3	18	31	45	47	0	15	28	36	50	62	1	4	7	11
Al	0.001	0.005	0.003	0.128	0.059	0.066	0.074	0.076	0.827	0.083	0.086	0.094	0.076	0.110	0.073	0.066	0.065	0.064
Ca	0.007	0.006	0.002	0.003	0.001	0.001	0.001	0.001	0.002	0.002	0.005	0.004	0.001	0.002	0.001	0.001	0.001	0.001
Fe	n.d.	0.003	0.001	0.003	0.001	0.001	0.001	0.001	0.010	0.003	0.003	n.d.	n.d.	n.d.	0.001	0.002	0.002	0.002
K	0.014	0.014	0.016	0.107	0.045	0.044	0.045	0.054	0.142	0.467	0.568	0.616	0.509	0.669	0.133	0.116	0.122	0.146
Mg	0.002	0.002	n.d.	0.003	n.d.	0.002	n.d.	n.d.	0.005	0.005	0.014	0.002	0.002	n.d.	n.d.	n.d.	n.d.	n.d.
Na	8.94	40.2	39.9	43.1	53.5	51.6	52.5	51.8	46.0	27.7	27.5	27.0	21.4	24.5	38.6	36.9	36.5	36.3
$\sum$S	n.d.	20.8	23.0	27.8	24.8	24.7	25.3	25.8	22.7	24.8	25.4	20.7	17.7	19.4	18.8	26.2	23.7	21.0
Si	0.021	0.055	0.051	0.573	0.144	0.114	0.105	0.107	4.25	9.88	9.98	9.93	7.41	8.65	1.03	1.10	1.14	1.17
$H_2(aq)$		62.9	135	1.80	13.7	2.66	35.3	15410	0.002	0.057	7.72	0.038	0.044	0.045	2.54	2.88	1.82	2.04
$H_2S(aq)$[a]		1.15	0.261	1.79	0.008	0.032	0.904	0.358	0.654	0.482	0.429	0.429	0.432	0.435	0.678	0.635	0.415	0.460

For dissolved gases, activity is assumed to be 1 since these species are neutral.
Failed measurement
  [a] Speciated using EQ3/6.

the behavior of sulfide in the reactive fluid through remobilization of S (not likely, since the dissolved sulfur content in this experiment is the lowest of all, see Fig. 2e) or uptake of small amounts of sulfur. Noteworthy is also the dissolved iron content, which is 10 times lower than in the olivine experiment. This can either mean that the system is so close to equilibrium that no Fe is released into the fluid, or that all Fe is quickly captured as magnetite. There is no indication for new magnetite formation during the experimental run based on XRD and VSM measurements. However, magnetic susceptibility before and after heating the sample to 650 °C (i.e., above the magnetite Curie temperature) showed that the solid reaction product had a stronger susceptibility signal after the heating cycle was complete. We have not examined the causes for the different behavior and a discussion of this phenomenon is outside the scope of the paper. It is still interesting to note that Fe apparently was reactive in the sulfidation experiment, such that the formation of new magnetite during heating was more favorable or that magnetite properties (e.g., grain size, magnetic domain distribution and size) may have changed.

4. Discussion

4.1. Models vs. experiments

Reaction path models for all experimental runs are given in Fig. 4a–d. For most runs the predicted reaction path does not comply with the

Fig. 3. Mineral stability in the Fe-O-S system. Plotted points come from all experiments. For discussion, see text.

observed mineral products (see also mineral overview provided in Table 3) as these reactions did not go to completion, so not all products were consumed (i.e. reaction progress Xi did not go to 1.0). However, modeled reaction directions were correct. Differences between models and reality could also be due to the model taking into account mineral stability instead of mineral formation temperature, which would lead to the prediction of minerals expected to grow at temperatures above our experimental conditions. Most likely, however, is the inability of thermodynamic models to properly predict mineral kinetics and the detection limit of methods such as XRD and SEM. The discrepancies in the magnetite-pyrite-pyrrhotite-hematite system will be discussed below.

The olivine reaction path model in EQ3/6 predicts serpentinization, as is observed. At the beginning of the run, a high w/r ratio favors the formation of pyrrhotite. This decreases the amount of H_2S, shifting the system towards magnetite stability. However, magnetite is not expected to form before reaction progress (Xi) reaches 0.40 (Fig. 4a), a point not reached in our experiment. Still, magnetite is observed while pyrrhotite is not, implying that S-activity in the fluid was too low to influence the far-from-equilibrium serpentinization reaction by the capture of Fe in a sulfide phase. One potential problem with this analysis is that the computed sulfide speciation, according to which roughly 1–5% of $\sum$S was present as H_2S, may have been an overestimation. Such an offset could be introduced by an in situ pH that is too low. Alternatively, magnetite was also supersaturated and prevented the nucleation and growth of pyrrhotite. The results of our speciation and solubility calculations do indeed suggest that magnetite was supersaturated and the levels of supersaturation are quite similar to that of pyrrhotite. It is hence conceivable that the pyrrhotite-forming reaction was not overstepped enough for the system to actually have the mineral form.

The troctolite experiment also predicts the observed serpentinization and shows a halted increase in pyrrhotite when magnetite becomes stable at Xi = 0.1 (Fig. 4b). This could imply that initially, pyrrhotite was stable in the reaction cell, decreasing H_2S-activity (through uptake of S), moving the system towards the lower right corner of the Fig. 3 where magnetite becomes the stable phase. Equilibrium between pyrrhotite and magnetite is therefore expected in the troctolite, but only the latter phase is observed; the grain size of relic pyrrhotite could be too small. Another possibility is that andradite stability overlies the magnetite and part of the pyrrhotite stability field when some SiO_2 is added to the system (Fig. 5) and it may thus have inhibited further pyrrhotite (and magnetite) formation.

The basalt reaction path model (Fig. 4c) predicts the observed formation of pyrite; the amount of formed sulfide (<28 mg) is however too small to be quantified using XRD. It also predicts the observed analcime; both pyrite and analcime disappear early in the reaction path, implying that the experiment was halted before this point (Xi = 0.03) was reached.
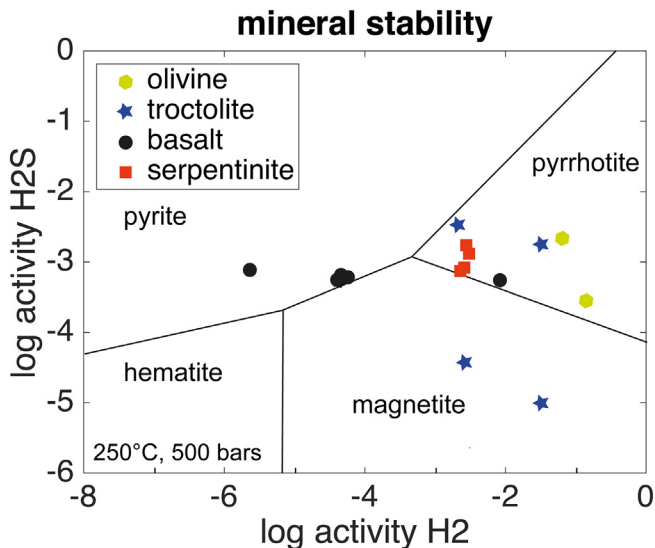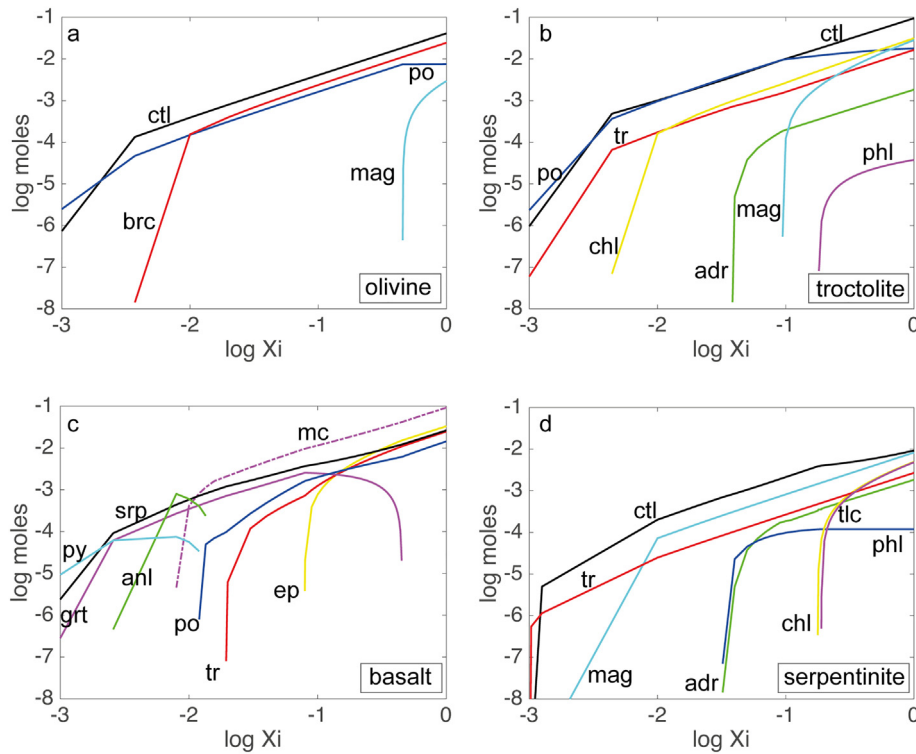
Fig. 4. GWB-based reaction path models for olivine (a), troctolite (b), basalt (c) and serpentinite (d) reaction with hydrothermal fluid showing the expected mineral assemblage with reaction progress, which runs from 0 to 1. Mineral abbreviations: adr = andradite; anl = analcime; brc = brucite, chl = chlorite; ctl = chrysotile; ep = epidote; grt = garnet; mag = magnetite; mc = microcline; phl = phlogopite; po = pyrrhotite; py = pyrite; srp = serpentine; tlc = talc; tr = tremolite. For discussion, see text.

The serpentinite experiment did not progress far since the fluid quickly reached equilibrium with the rock (Fig. 2d). This means that we should compare the reaction path model at Xi = 0.01 with our observations, where only serpentine, magnetite and possibly some small amounts of tremolite are predicted (Fig. 4d). Except for the tremolite, this is in line with our observations. It is worth to note that, despite the high amount of sulfur added, no sulfide phase is predicted, even though the activity-activity plot shows the reaction within the pyrrhotite stability field. This might be a similar overestimation of the activity of H2S as in the olivine run, as pyrrhotite is not predicted in the reaction path model, or pyrrhotite formation kinetics may have been sluggish.

We did not increase the w/r ratio further however, as this would leave us with too little solids to analyze.

Despite all predicted S-bearing phases using induced H2 and H2S activity, only basalt succeeded in the net capture of sulfide. H2S-activity in all the other runs must therefore have been lower than estimated in the EQ3/6 software. We deduced the percentage of total sulfur present as H2S from speciation calculations on the 250 °C reactive fluid using EQ6 software. These highly pH dependent speciation calculations may cause a slight error since starting fluid pH at 25 °C could not be

Table 3
Diagram with expected and observed mineralogy. The diagram shows which minerals are expected when the reaction goes to completion (blue), which are actually observed (yellow) and which are both modeled and observed (green). The numbers represent saturation indices for predicted minerals at the predicted final reaction progress (Xi mentioned above each column) of each run.

Replacive minerals	Abbreviation	Xi=.05 Olivine	Xi=1 Troctolite	Xi=.1 Basalt	Xi=.01 Serpentinite
Serpentine	srp	18.9	29.1		16.3
Brucite	brc	4.64			
Magnetite	mag	6.42	11.7		4.66
Pyrite	py			5.97	
Pyrrhotite	po	2.47	3.25	4.85	
Epidote	ep			19.1	
Chlorite	chl		50.0	36.7	24.9
Tremolite	tr		69.2	49.5	32.2
Phlogopite	phl			24.7	16.0
Analcime	anl			3.72	
Andradite	adr		29.0	24.9	9.15
Microcline	mc			4.63	

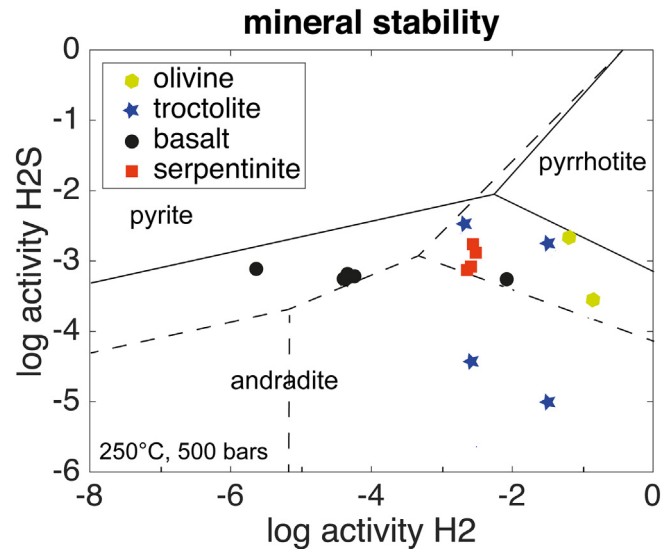|	
Sredicted at end of reaction (see Xi)	
Seen	
Both	

Fig. 5. Andradite stability field overlaps with magnetite, hematite and parts of the pyrrhotite and pyrite field. Si-addition to the system has severe results in reaction products.

measured, only inferred from the added Na_2S as dissolution and equilibration with Na_2S took place during heating and start of the water-rock interaction.

4.2. Silica activity

In those experiments including serpentinization, dissolved silica content was of great importance. Pure olivine serpentinization occurs under low Si-activity and will result in the additional formation of brucite while higher Si-activity (for example through the initial presence of pyroxenes) leads to serpentine as only reaction product (Frost and Beard, 2007). The dissolving minerals in the troctolite experiment increased the Si-content in the system and the large amount of andradite (instead of other Ca-silicates such as Si-richer tremolite or chlorite) showed that this is a factor that should not be ignored. Besides increased Si and Ca concentration (compare Fig. 2a and b), in situ pH should be above 9 and silica activity should not exceed 2.5 mmol/L because Ca-Fe silicates besides andradite might become stable (Beard and Hopkinson, 2000). Andradite is only observed in the troctolite experiment and may impede sulfide formation, as it decreases the availability of Fe for sulfides.

To analyze the stability of andradite, a similar diagram to Fig. 3 can be plotted that includes ions such as Ca, Si, Al and Mg. After suppressing non-observed phases (everything except plagioclase, saponite, andradite, serpentine, chlorite, brucite, olivine and magnetite), andradite plots right where the hematite, magnetite and part of the pyrrhotite stability field are in the absence of silica (Fig. 5). The presence of both magnetite and andradite implies that the system has experienced a shift in Si-activity, which is confirmed by Fig. 2b and implies that magnetite must postdate andradite. We already know from fluid measurements (Fig. 2e) that dissolved sulfur content also evolves: the small initial decreasing S-content in the fluid can be explained by formation of pyrrhotite while a later re-dissolution is shown by sulfur release back into the fluid. Dissolved H_2 and H_2S contents (Fig. 3) show that this trend is probably due to an increased H_2-production upon olivine serpentinization. The Fe released from pyrrhotite re-dissolution was probably captured in magnetite. However, the elevated Si content in this fluid also allows the formation of an iron-silicate phase: andradite. One could argue that by this, magnetite crystallization is partially inhibited until Si-activity dropped due to precipitation.

The presence of andradite related to serpentinization is discussed by several authors (e.g. Bideau et al., 1991; Frost, 1985; Früh-Green et al., 1996; Ghosh et al., 2017; Plümper et al., 2014). It is even observed in Hole 1309D where our troctolite starting material was retrieved, although at different depth; Frost et al. (2008) reported garnet growth in veins, surrounded by prehnite on the contact with anorthite, implying that the garnet formed below 350 °C by simple 'desilicification' of plagioclase instead of Ca-metasomatism. A similar process is expected in the troctolite experiment, where andradite results from dissolution of plagioclase and release of Si instead of addition of Ca to the system. Aluminum can be taken out of solution by chlorite precipitation, but elevated Al contents and the limited amount of expected chlorite show that this did not occur. This could be related to a batch experiment's limited ability to mimic a natural flow-through system, as there is no constant replenishment of fluid. Instead, saponite is observed as a possible Al-bearing phase, but since this clay mineral is metastable, the presence of chlorite is still expected.

Likewise, in the basalt experiment chlorite is predicted to form but could not be detected. Chlorite is known as a phase that is difficult to synthesize directly from hydrothermal fluids (e.g., Small et al., 1992); hence, sluggish kinetics can account for its absence. Other silicate phases (such as epidote or microcline) are predicted to form along the reaction paths, but empirical data indicate that higher temperatures are often required for their formation (e.g., Bird and Spieler, 2004). Another possibility is that chlorite has been overlooked in the measurements. Indeed, the mass of chlorite estimated from the amount of Ca

released to the fluid and assuming that it takes up the left-behind Al is <0.1 g (i.e., <2 wt% of solids).

We did find clay minerals in the solid reaction products this run, which probably formed metastably.

4.3. Sulfide stability in serpentinites

Water-to-rock ratio is crucial to sulfide stability, as low water fluxes and reducing conditions will destabilize sulfide minerals, whereas high water fluxes result in relatively oxidizing conditions and allow for pyrite and high sulfur-fugacity phases (Frost, 1985; Klein and Bach, 2009). These more oxidized conditions are common for basalt-hosted hydrothermal systems (Seyfried Jr and Ding, 1995; data overview of Kawasumi and Chiba, 2017) or for carbonated serpentinites, where the system is buffered at a higher oxygen fugacity than pure serpentinization through equilibrium with magnesite (Klein and Garrido, 2011). Lower w/r ratios result in high metal sulfides or even native metals (Frost, 1985). Examples of both types can be found at the Iberia Margin, where Beard and Hopkinson (2000) discovered pentlandite, heazlewoodite and awaruite in deeper sections, and andradite, magnesite and even hematite close to fracture zones.

It is noteworthy that our serpentinite experiment had the highest w/r ratio of all but shows no signs of sulfides. This must mean that the total sulfur input was too low in this reducing system to allow for sulfide formation. Therefore, the w/r ratio is only deterministic for sulfide formation as long as it puts the system at a higher oxidation state. Instead, magnetite is observed in this run, which shows that the activity of H_2S was again lower than predicted by the model. This same process occurred in the olivine experiment, where fO_2 remains low because of H_2-production and all sulfur stays in solution as HS^-, not precipitating any sulfides but magnetite instead (cf. Alt and Shanks III, 1998). The basalt experiment on the other hand had the lowest w/r ratio and was the easiest to sulfidize, even though in absolute numbers, the least sulfur was added to this system. This shows that S-activity is more important than the absolute S-content, and it shows the readiness of basalt to sulfidize compared to the other tested lithologies, which were more reducing and produced more H_2 during reaction with hydrothermal fluid (Fig. 3). In natural systems, most large sulfide deposits can also be found in mafic rock (TAG, Snake Pit, Lucky Strike), not ultramafic.

4.4. Comparison to natural examples: implications for the formation of massive sulfide deposits in different lithologies

We compare our products from reacting different rock types under similar reaction conditions with observations from natural samples. In the Atlantis Massif (30°N, MAR), serpentinites, gabbros and troctolites have been discovered close to an actively venting system (Delacour et al., 2008a, 2008b). The southern wall is located below the Lost City Hydrothermal Field and shows evidence for alteration under oxidizing conditions: serpentinized peridotite and gabbros in this area are depleted in sulfur and show high $\delta^{34}S_{sulfide}$ values (up to +12‰); sulfates are more abundant than sulfides (Delacour et al., 2008a). This implies leaching of magmatic sulfides and oxidation of the remnant sulfide minerals, resulting in sulfate and some pyrite. At the central dome, less seawater influence is observed (Delacour et al., 2008b). Here, gabbro and troctolite samples at depth showed mainly primary magmatic sulfides, whereas serpentinized samples closer to the seafloor showed higher sulfur contents and their isotopic signature reflects input of hydrothermal sulfides from leaching of mafic rocks as well as sulfide input from thermochemical sulfate reduction. This is thought to come from seawater-gabbro interaction, and subsequent serpentinization with this fluid. Similarly high total sulfur (up to 1 wt%) and positive $\delta^{34}S_{sulfide}$ values are also observed at the MARK area at 23°N (Alt and Shanks III, 2003) and the MAR fracture zone at 15°N (Alt et al., 2007; Bach et al., 2004). Mafic-hosted hydrothermal systems such as TAG also have heavy sulfur isotopes up to +6‰ (Herzig et al., 1998) and are rich in

pyrite (Patten et al., 2016; Zierenberg et al., 1984). Although the venting temperatures at TAG are >250 °C, the dominant formation of hydrothermal pyrite is similar to the results of our basalt experiment.

Unfortunately, the Atlantis Massif or MAR examples cannot provide more insight in troctolite sulfidation, because only leaching of magmatic sulfides has been observed (Atlantis Massif) or the magmatic signature is preserved (MAR, Alt et al., 2007). However, the gabbroic section in the southern wall of the Atlantis Massif is more prone to pyrite formation than serpentinite, even though the latter formed under relatively high fO_2 conditions (Delacour et al., 2008a). The lack of sulfides in our olivine and serpentinite experiments compares nicely to this observation. This apparent lack of sulfide formation may be due to the relatively low H_2S activity during serpentinization. Klein and Bach (2009) showed that even though the reactions of pentlandite to magnetite and heazlewoodite entails a desulfidation of the ultramafic rock, the associated H_2S activity of the interacting fluid is low (around 1 mM), which is consistent with typical H_2S concentrations in high-temperature ultramafic-hosted vents, such as Rainbow. But in the exposures of stockwork in the Rainbow hydrothermal vent field, replacement of serpentinite by pyrite and pyrrhotite (along with magnetite) has been documented (Marques et al., 2006). It is likely that the stockwork mineralization at Rainbow developed in an environment, in which hot (>360 °C) upwelling hydrothermal solutions mixed with seawater entrained in the subseafloor. In our simple batch experiment at 250 °C, sulfides did not form, although there was thermodynamic drive for pyrrhotite formation. More experimental work is required to examine the mechanisms of sulfidization of ultramafic rocks in seafloor hydrothermal systems.

5. Summary

Reaction of olivine, troctolite, basalt and serpentinite with a fluid bearing 20 mmol/kg H_2S at 250 °C and 400 bars did not always result in the expected sulfidation of rock. The olivine experiment showed partial serpentinization (roughly 5%) with the formation of magnetite instead of the thermodynamically predicted pyrrhotite; this might relate to the sluggish formation kinetics of the latter phase. The serpentinite experimental run was close to equilibrium with the fluid from the start and only showed minor growth of magnetite. The troctolite resulted in full hydration of olivine, while all plagioclase was transformed into andradite and clays. Once again, the presence of predicted pyrrhotite contradicted observations. A dip in sulfur content in the fluid and a later sulfur release suggests that pyrrhotite might have been present temporarily, being replaced later on by magnetite.

Only in the basalt experiment a sulfide phase was formed. Euhedral pyrite crystals were detected on the dissolving plagioclase and pyroxene minerals, as well as the Na-zeolite analcime. Although this run had the lowest w/r ratio, its oxidized nature allowed for pyrite to precipitate. The other lithologies imposed conditions too reducing for pyrite to form. The activity of SiO_2 and H_2S proved very important for the sulfidation of the system. In the troctolite experiment, andradite stability overlapped with magnetite and pyrrhotite, possibly inhibiting their formation. The high amount of added sulfur did not counteract this process. Oxygen fugacity also proved to be important, as the more oxidizing basalt was the only one to produce pyrite despite the higher amounts of H_2S added to the other lithologies. This may be explained by higher sulfur fugacity under oxidizing conditions being more important than the total amount of dissolved sulfide.

This study presents the first evidence for replacive pyrite formation (as Fe is leached from the rock and captured in pyrite), which is observed in hydrothermal stockwork zones (e.g., in the TAG active hydrothermal system).

Basaltic rock compositions appear to have a higher affinity for sulfidation than more olivine-rich lithologies. Further studies are needed to explain the apparent sulfidization of serpentinized peridotite by fluids with low sulfide contents.

References

Adamides, N.G., 2010. Mafic-dominated volcanogenic sulphide deposits in the Troodos ophiolite, Cyprus Part 2 – a review of generic models and guides for exploration. Applied Earth Science 119 (4), 193–204.

Alt, J.C., Shanks, W.C., 2011. Microbial sulfate reduction and the sulfur budget for a complete section of altered oceanic basalts, IODP Hole 1256 (eastern Pacific). Earth and Planetary Science Letters 310, 73–83.

Alt, J.C., Shanks III, W.C., 1998. Sulfur in serpentinized oceanic peridotites: Serpentinization processes and microbial sulfate reduction. Journal of Geophysical Research 103 (B5), 9917–9929.

Alt, J.C., Shanks III, W.C., 2003. Serpentinization of abyssal peridotites from the MARK area, Mid-Atlantic Ridge: sulfur geochemistry and reaction modeling. Geochimica et Cosmochimica Acta 64 (4), 641–653.

Alt, J.C., Shanks III, W.C., Bach, W., Paulick, H., Garrido, C.J., Beaudoin, G., 2007. Hydrothermal alteration and microbial sulfate reduction in peridotite and gabbro exposed by detachment faulting at the Mid-Atlantic Ridge, 15°20′N (ODP Leg 209): a sulfur and oxygen isotope study. Geochemistry, Geophysics, Geosystems 8 (8), Q08002. https://doi.org/10.1029/2007GC001617.

Alt, J.C., Schwarzenbach, E.M., Früh-Green, G.L., Shanks III, W.C., Bernasconi, S.M., Garrido, C.J., Crispini, L., Gaggero, L., Padrón-Navarta, J.A., Marchesi, C., 2013. The role of serpentinites in cycling of carbon and sulfur: Seafloor serpentiniation and subduction metamorphism. Lithos 178, 40–54.

Bach, W., Garrido, C.J., Paulick, H., Harvey, J., Rosner, M., 2004. Seawater-peridotite interactions: first insights from ODP Leg 209, MAR 15°N. Geochemistry, Geophysics, Geosystems 5 (9), Q09F26. https://doi.org/10.1029/2004GC000744.

Beard, J.S., Hopkinson, L., 2000. A fossil, serpentinization-related hydrothermal vent, Ocean Drilling Program Leg 173, Site 1068 (Iberia Abyssal Plain): some aspects of mineral and fluid chemistry. Journal of Geophysical Research 105 (B7), 16527–16539.

Bideau, D., Hebert, R., Hekinian, R., Cannat, M., 1991. Metamorphism of deep-seated rocks from The Garrett Ultrafast Transform (East Pacific Rise Near 13°25′S). Journal of Geophysical Research 96 (B6), 10079–10099.

Bird, D.K., Spieler, A.R., 2004. Epidote in geothermal systems. In: Liebscher, A., Frantz, G. (Eds.), Epidotes. Reviews in Mineralogy and Geochemistry, Mineralogical Society of America, Geochemical Society vol. 56, pp. 235–300.

Bischoff, J.L., Dickson, F.W., 1975. Seawater-basalt interaction at 200 °C and 500 bars: implications for origin of sea-floor heavy-metal deposits and regulation of seawater chemistry. Earth and Planetary Science Letters 25, 385–397.

Czamanske, G.K., Moore, J.G., 1977. Composition and phase chemistry of sulfide globules in basalt from the Mid-Atlantic Ridge rift valley near 37°N lat. Geological Society of America Bulletin 88, 587–599.

Delacour, A., Früh-Green, G.L., Bernasconi, S.M., Kelley, D.S., 2008a. Sulfur in peridotites and gabbros at Lost City (30°N, MAR): implications for hydrothermal alteration and microbial activity during serpentinization. Geochimica et Cosmochimica Acta 72, 5090–5110.

Delacour, A., Früh-Green, G.L., Bernasconi, S.M., 2008b. Sulfur mineralogy and geochemistry of serpentinites and gabbros of the Atlantis Massif (IODP Site U1309). Geochimica et Cosmochimica Acta 72, 5111–5127.

Frost, B.R., 1985. On the stability of sulfides, oxides, and native metals in serpentinite. Journal of Petrology 26 (1), 31–63.

Frost, B.R., Beard, J.S., 2007. On silica activity and serpentinization. Journal of Petrology 48, 1351–1368.

Frost, B.R., Beard, J.S., McCaig, A., Condliffe, E., 2008. The formation of micro-rodingites from IODP Hole U1309D: key to understanding the process of serpentinization. Journal of Petrology 49, 1579–1588.

Früh-Green, G.L., Plas, A., Lécuyer, C., 1996. Petrologic and stable isotope constraints on hydrothermal alteration and serpentinization of the EPR shallow mantle at Hess Deep (Site 895). In: Mével, C., Gillis, K.M., Allen, J.F., Meyer, P.S. (Eds.), Proceedings of the Ocean Drilling Program. Scientific Results vol. 147.

Ghosh, B., Morishita, T., Ray, J., Tamura, A., Mizukami, T., Soda, Y., Ovung, T.N., 2017. A new occurrence of titanian (hydro)andradite from the Nagaland ophiolite, India: implications for element mobility in hydrothermal environments. Chemical Geology 457, 47–60.

Godard, M., Luquot, L., Andreani, M., Gouze, P., 2013. Incipient hydration of mantle lithosphere at ridges: a reactive-percolation experiment. Earth and Planetary Science Letters 371-372, 92–102.

Hannington, M.D., Galley, A.G., Herzig, P.M., Petersen, S., 1998. Comparison of the TAG mound and the stockwork complex with Cyprus-type massive sulfide deposits. In: Herzig, P.M., Humphris, S.E., Miller, D.J., Zierenberg, R.A. (Eds.), Proceedings of the Ocean Drilling Program. Scientific Results vol. 158.

Herzig, P.M., Petersen, S., Hannington, M.D., 1998. Geochemistry and sulfur-isotopic composition of the TAG hydrothermal mound, Mid-Atlantic Ridge, 26°N. In: Herzig, P.M., Humphris, S.E., Miller, D.J., Zierenberg, R.A. (Eds.), Proceedings of the Ocean Drilling Program. Scientific Results vol. 158.

Humphris, S.E., Herzig, P.M., Miller, D.J., Alt, J.C., Becker, K., Brown, D., Brügmann, G., Chiba, H., Fouquet, Y., Gemmell, J.B., Guerin, G., Hannington, M.D., Holm, N.G., Honnorez, J.J., Itturino, G.J., Knott, R., Ludwig, R., Nakamura, K., Petersen, S., Reysenbach, A.-L., Rona, P.A., Smith, S., Sturz, A.A., Tivey, M.K., Zhao, X., 1995. The internal structure of an active sea-floor massive sulphide deposit. Nature 377, 713–716.

Jarosewich, E., Nelen, J.A., Norberg, J.A., 1980. Reference Samples for Electron Microprobe Analysis. Geostandards Newsletter 4 (1), 43–47.

Johnson, J.W., Oelkers, E.H., Helgeson, H.C., 1992. Supcrt92: a software package for calculating the standard molal thermodynamic properties of minerals, gases, aqueous species, and reactions from 1 to 5000 bar and 0 to 1000 °C. Computers and Geosciences 18 (7), 899–947.

Kawasumi, S., Chiba, H., 2017. Redox state of seafloor hydrothermal fluids and its effect on sulfide mineralization. Chemical Geology 451, 25–37.

Klein, F., Bach, W., 2009. Fe-Ni-Co-O-S phase relations in peridotite-seawater interactions. Journal of Petrology 50 (1), 37–59.

Klein, F., Garrido, C.J., 2011. Thermodynamic constraints on mineral carbonation of serpentinized peridotite. Lithos 126, 147–160.

Klein, F., Bach, W., Jöns, N., McCollom, T., Moskowitz, B., Berquó, T., 2009. Iron partitioning and hydrogen generation during serpentinization of abyssal peridotites from 15°N on the Mid-Atlantic Ridge. Geochimica et Cosmochimica Acta 73 (6868-6803).

Klein, F., Grozeva, N.G., Seewald, J.S., McCollum, T.M., Humphris, S.E., Berquó, T.S., Kahl, W.-A., 2015. Experimental constrains on fluid-rock reactions during incipients serpentinization of harzburgite. American Mineralogist 100 (4), 991–1002.

Marques, A.F.A., Barriga, F., Chavagnac, V., Fouquet, Y., 2006. Mineralogy, geochemistry, and Nd isotope composition of the Rainbow hydrothermal field, Mid-Atlantic Ridge. Mineralium Deposita 41, 52–67.

Marques, A.F.A., Barriga, F.J.A.S., Scott, S.D., 2007. Sulfide mineralization in an ultramafic-rock hosted seafloor hydrothermal system: from serpentinization to the formation of Cu–Zn–(Co)-rich massive sulfides. Marine Geology 245, 20–39.

Melchert, B., Devey, C.W., German, C.R., Lackschewitz, K.S., Seifert, R., Walter, M., Mertens, C., Yoerger, D.R., Baker, E.T., Paulick, H., Nakamura, K., 2008. First evidence for high-temperature "off-axis" venting of deep crustal heat: the Nibelungen hydrothermal field, Southern Mid-Atlantic Ridge. Earth and Planetary Science Letters 275, 61–69.

Mottl, M.J., Holland, H.D., 1978. Chemical exchange during hydrothermal alteration of basalt by seawater: I. Experimental results for major and minor components of seawater. Geochimica et Cosmochimica Acta 42, 1103–1115.

Mottl, M.J., Holland, H.D., Corr, R.S., 1979. Chemical exchange during hydrothermal alteration of basalt by seawater: II. Experimental results for Fe, Mn and sulfur species. Geochimica et Cosmochimica Acta 43, 869–884.

Patten, C.G.C., Pitcairn, I.K., Teagle, D.A.H., Harris, M., 2016. Sulphide mineral evolution and metal mobility during alteration of the oceanic crust: insights from ODP Hole 1256D. Geochimica et Cosmochimica Acta 193, 132–159.

Paulick, H., Bach, W., Godard, M., De Hoog, J.C.M., Suhr, G., Harvey, J., 2006. Geochemistry of abyssal peridotites (Mid-Atlantic Ridge, 15°20′N, ODP Leg 209): implications for fluid/rock interaction in slow spreading environments. Chemical Geology 234, 179–210.

Peach, C.L., Mathez, E.A., Keays, R.R., 1990. Sulfide melt silicate melt distribution coefficients for noble-metals and other chalcophile elements as deduced from

MORB – implications for partial melting. Geochimica et Cosmochimica Acta 54, 3379–3389.

Peters, M., Strauss, H., Farquhar, J., Ockert, C., Eickmann, B., Jost, C.L., 2010. Sulfur cycling at the Mid-Atlantic Ridge: a multiple sulfur isotope approach. Geomical Geology 269, 180–196.

Petersen, S., Kuhn, K., Kuhn, T., Augustin, N., Hékinian, R., Franz, L., Borowski, C., 2009. The geological setting of the ultramafic-hosted Logatchev hydrothermal field (14°4′N, Mid-Atlantic Ridge) and its influence on massive sulfide formation. Lithos 112, 40–56.

Plümper, O., Beinlich, A., Bach, W., Janots, E., Austrheim, A., 2014. Garnets within geode-like serpentinite veins: implications for element transport, hydrogen production and life-supporting environment formation. Geochimica et Cosmochimica Acta 141, 454–471.

Schwarzenbach, E.M., Früh-Green, G.L., Bernasconi, S.M., Alt, J.C., Shanks III, W.C., Gaggero, L., Crispini, L., 2012. Sulfur geochemistry of peridotite-hosted hydrothermal systems: comparing the Ligurian ophiolites with oceanic serpentinites. Geochimica et Cosmochimica Acta 91, 283–305.

Seewald, J.S., Seyfried, W.E., 1990. The effect of temperature on metal mobility in subseafloor hydrothermal systems: constraints from basalt alteration experiments. Earth and Planetary Science Letters 101, 388–403.

Seward, T.M., Williams-Jones, A.E., Migdisov, A.A., 2014. The Chemistry of Metal Transport and Deposition by Ore-forming Hydrothermal Fluids. 2nd edition. Treatise Geochemistry 13 pp. 29–57.

Seyfried Jr., W.E., Ding, K., Humphris, S.E., Zierenberg, R., Mullineaux, L., Thomson, R., 1995. Phase equilibria in subseafloor hydrothermal systems: a review of the role of redox, temperature, pH and dissolved Cl on the chemistry of hot spring fluids at Mid-Ocean Ridge. Seafloor Hydrothermal Systems: Physical, Chemical, Biological and Geological Interactions. Geophysical Monogram 91. American Geophysical Union, pp. 248–272.

Seyfried Jr., W.E., Dibble Jr., W.E., 1980. Seawater-peridotite interaction at 300 °C and 500 bars: implications for the origin of oceanic serpentinites. Geochimica et Cosmochimica Acta 44, 309–321.

Shanks II, W.C., Bischoff, J.L., Rosenbauer, R.J., 1981. Seawater sulfate reduction and sulfur isotope fractionation in basaltic systems: interaction of seawater with fayalite and magnetite at 200–350 °C. Geochimica et Cosmochimica Acta 45 (11), 1977–1995.

Shibuya, T., Yoshizaki, M., Masaki, Y., Suzuki, K., Takai, K., Russell, M.J., 2013. Reactions between basalt and CO_2-rich seawater at 250 and 350 °C, 500 bars: implications for the CO_2 sequestration into the modern oceanic crust and the composition of hydrothermal vent fluid in the CO_2-rich early ocean. Chemical Geology 359, 1–9.

Sleep, N.H., Meibom, A., Fridriksson, Th., Coleman, R.G., Bird, D.K., 2004. H_2-rich fluids from serpentinization: geochemical and biotic implications. Proceedings of the National Academy of Sciences of the United States of America 101 (35), 12818–12823.

Small, J.S., Hamilton, D.L., Habesch, S., 1992. Experimental simulation of clay precipitation within reservoir sandstones 1: techniques and examples. Journal of Sedimentary Research 62 (3), 508–519.

Smith, D.K., Escartin, J., Schouten, H., Cann, J.R., 2008. Fault rotation and core complex formation: significant processes in seafloor formation at slow-spreading mid-ocean ridges (Mid-Atlantic Ridge, 13–15°N). Geochemistry, Geophysics, Geosystems 9 (3), Q03003. https://doi.org/10.1029/2007GC001699.

Wolery, T.W., Jarek, R.L., 2003. Software User's Manual EQ3/6, Version 8.0. Sandia National Laboratories, Albuquerque, NM, USA.

Zierenberg, R.A., Shanks III, W.C., Bischoff, J.L., 1984. Massive sulfide deposits at 21°N, East Pacific Rise: chemical composition, stable isotopes, and phase equilibria. Geological Society of America Bulletin 95, 922–929.

Zierenberg, R.A., Shanks III, W.C., Seyfried Jr., W.E., Koski, R.A., Strickler, M.D., 1988. Mineralization, alteration, and hydrothermal metamorphism of the ophiolite-hosted Turner-Albright sulfide deposit, Southwestern Oregon. Journal of Geophysical Research 93 (B5), 4657–4674.